

# Capillary dynamics of coupled spherical-cap droplets

E. A. THEISEN<sup>1</sup>, M. J. VOGEL<sup>1</sup>, C. A. LÓPEZ<sup>2</sup>,  
A. H. HIRSA<sup>2</sup> AND P. H. STEEN<sup>1</sup>

<sup>1</sup>School of Chemical and Biomolecular Engineering, Cornell University, Ithaca, NY 14853, USA

<sup>2</sup>Department of Mechanical, Aerospace and Nuclear Engineering, Rensselaer Polytechnic Institute, Troy, NY 12180, USA

(Received 3 November 2006 and in revised form 15 February 2007)

Centre-of-mass motions of two coupled spherical-cap droplets are considered. A model with surface tension and inertia that accounts for finite-amplitude deformations is derived in closed form. Total droplet volume  $\lambda$  and half-length  $L$  of the tube that connects the droplets are the control parameters. The model dynamics reside in the phase-plane. For lens-like droplets  $\lambda < 1$ , and for any  $L$  there is a single steady state about which the droplets vibrate with limit-cycle behaviour. For  $\lambda > 1$ , the symmetric state loses stability (saddle point) and new antisymmetric steady states arise about which limit-cycle oscillations occur. These mirror states – big-droplet up or big-droplet down – are also stable. In addition, there are large finite-amplitude ‘looping’ oscillations corresponding to limit cycles that enclose both steady states in the phase-plane. All three kinds of oscillations are documented in an experiment that sets the system into motion by ‘kicking’ one of the droplets with a prescribed pressure-pulse. Model predictions for frequencies are consistent with observations. Small-amplitude predictions are placed in the wider context of constrained Rayleigh vibrations. A model extension to account for the small but non-negligible influence of viscosity is also presented.

---

## 1. Overview

Liquid droplets tend to spherical shapes under the action of surface tension. The vibration of a sphere is a classical example of the competition between liquid inertia and capillarity. As summarized by Lamb (1932), Lord Rayleigh (1879) predicted the frequency of small oscillations (mode  $n$ ),

$$\omega_n^2 = n(n-1)(n+2)(\sigma/\rho r^3), \quad (1.1)$$

where  $\sigma$ ,  $\rho$  and  $r$  are surface tension, liquid density and radius of the undeformed sphere, respectively (see also Webb 1880). The frequencies  $\omega_0 = 0$  and  $\omega_1 = 0$  are due to translational invariance and the constant-volume constraint, respectively. The lowest non-zero frequency  $\omega_2$  plays an important role in applications. The prediction of Rayleigh has been verified in experiment and its relevance well-documented (e.g. Trinh & Wang 1982 and Bisch, Lasek & Rodot 1982).

Suppose that the Rayleigh droplet is now constrained by pinning it on a circle of contact (figure 1*a, b*). How will the constraint influence the frequency of oscillation? Will it go up or down? A reasonable answer might be that the constrained droplet will oscillate faster, just as a shorter violin string has higher pitch. This reasoning and the conclusion would be correct if one restricts to a fixed mode; that is, pinning the surface

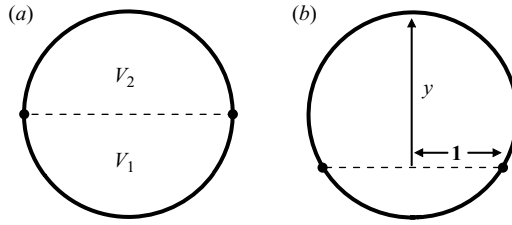


FIGURE 1. Pinning along a circle-of-contact (dotted line) varies in position from (a) the equator ( $V_1 - V_2 = 0$ ) to (b) the southern hemisphere ( $V_1 - V_2 < 0$ ).

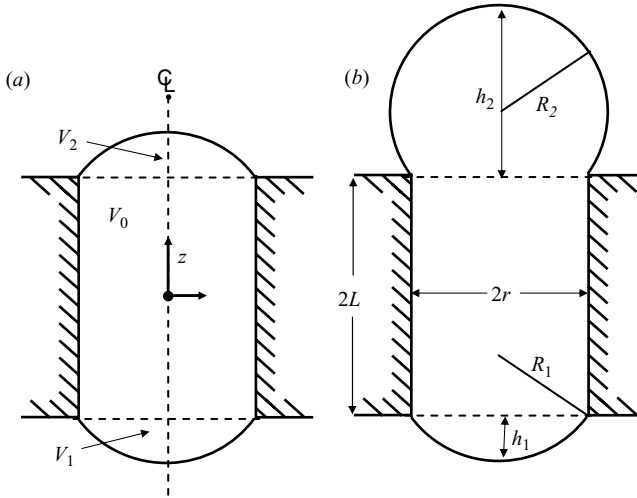


FIGURE 2. Schematic of coupled droplets pinned at tube ends of radius  $r$ .  $V_1$  and  $V_2$  are protruding volumes. Typical equilibria for (a)  $V_1 + V_2 < (4/3)\pi r^3$  and (b)  $V_1 + V_2 > (4/3)\pi r^3$ . Equilibrium occurs for menisci with equal curvatures,  $R_1 = R_2$ .

increases the frequency for any particular mode. On the other hand, if all modes are allowed, the situation is not so straightforward. It turns out that pinning can ‘activate’ the translational mode, raising its frequency from zero and introducing a slow oscillation. The slow frequency  $\omega_2^*$  depends on where the pinning circle is placed (figure 1). We report below (the  $L = 0$  limit of (4.1)) that  $\omega_2^*/\omega_2 = \sqrt{3}(y - 1/y)/4$  where  $y \geq 1$  is the distance from the north pole to the constraining circle scaled by the radius of the constraint (figure 1b). Thus, the slow frequency increases monotonically from zero for a pinned-equator constraint (figure 1a) to infinity for a pinned point at the south pole. In particular, the translational-mode frequency crosses the unconstrained slow frequency ( $\omega_2^*/\omega_2 = 1$ ) at  $y_c \equiv (2 + \sqrt{7})/\sqrt{3} \sim 2.68$ . Hence, according to our model, the correct answer depends on where the pinned constraint is placed. The emergence of a linear, low-frequency centre-of-mass oscillation in a related problem has been reported by Strani & Sabetta (1984). The translational mode introduced by the pinned circular constraint has not been studied before, however, as far as we are aware.

The above geometry-of-constraint is generalized in two ways in our study. First, two sub- or super-hemispherical caps can be joined at the constraining circle giving a non-spherical overall shape. Second, the pinning circle can be ‘inflated’ to be a cylindrical tube of length  $2L$  with spherical caps pinned to each of the tube ends (figure 2). This family of undeformed capillary surfaces is characterized by two

control parameters: the sum of spherical-cap volumes ( $V_1 + V_2$ ) and the connection half-length  $L$ . Figure 2 shows symmetric and antisymmetric equilibria (inter-droplet pressures equal) distinguished by  $V_1 + V_2 < (4/3)\pi r^3$  (figure 2a) or  $V_1 + V_2 > (4/3)\pi r^3$  (figure 2b).

The translational motion of the droplet–droplet system is modelled by restricting to spherical-cap shapes. The benefit of this approximation is that finite-amplitude dynamics become tractable. The motions are described by a two-dimensional system while Rayleigh’s infinitesimal motions are described by a partial differential equation. For the purposes of this paper, the validity of the approximation is tested by comparing with experiment.

Motivation for this study comes from practical applications. Two pressure-coupled droplets have a double-welled surface energy landscape. With a mechanism to trigger from one well to another, such as with an electro-osmotic pump placed in the tube (Vogel, Ehrhard & Steen 2005), the system becomes active. A number of applications that exploit capillary bi-stability are under development. These include optical micro-lens devices (López, Lee & Hirsá 2005). For these, understanding the dynamics of the droplet–droplet configuration and especially the lowest frequency mode is important.

Droplet motions dominated by inertia and surface tension are generally also influenced by liquid viscosity. Even though the Reynolds number is order one hundred, viscous effects are non-negligible according to experiment. The proposed inviscid model of the translational-mode dynamics is readily modified to include viscous damping.

## 2. Dynamical model

Let  $z_c$  be the centre-of-mass for the total liquid volume (figure 2), in the tube and both droplets,  $V_T = V_0 + V_1 + V_2$ . Newton’s law takes the form

$$\frac{d}{dt} \left( \rho V_T \frac{dz_c}{dt} \right) = F_\sigma + F_\mu. \quad (2.1)$$

Owing to axisymmetry, the net force  $F = F_\sigma + F_\mu$  acting on the control volume is in the axial direction,  $F\mathbf{e} = \int_{\partial V_T} \mathbf{T}\mathbf{n} \, dA$ , where  $\mathbf{T} = -p\mathbf{1} + 2\mu\mathbf{D}$  is the stress tensor,  $\mu$  is the viscosity,  $\mathbf{D}$  the symmetric part of the velocity gradient tensor,  $\mathbf{e}$  the axial unit vector and  $\mathbf{n}$  the unit normal. The net force splits into a capillary  $F_\sigma$  and a viscous part  $F_\mu$  according to the split between pressure and deviatoric stress using the assumption of a stress-free liquid/gas interface. The pressure contribution, from the spherical-cap droplets of radius  $R_i$ , is evaluated by the Young–Laplace relationship,  $p_i = 2\sigma/R_i$  for  $i = 1, 2$ , to yield  $F_\sigma = \pi r^2(p_1 - p_2) = 2\pi r^2\sigma(1/R_1 - 1/R_2)$ . The viscous part arises due to tractions along the tube wall  $\partial V_0$  and can be written  $F_\mu = 2\mu \int_{\partial V_0} \mathbf{e}\mathbf{D}\mathbf{n} \, dA = 2\mu(4\pi rL/\tau)f$  where  $f$  is the dimensionless viscous force and  $\tau$  a characteristic time scale. It is convenient to scale all lengths with  $r$ , volumes with  $(4/3)\pi r^3$  and to choose a time scale to balance the inertia and capillary terms,  $\tau^2 \equiv \rho r^3/\sigma$ . Henceforth, unless otherwise noted, variables will be dimensionless. We will use the same symbol for scaled as for previously unscaled variables. Substitute forces into (2.1), use the scales just defined, and rearrange to find

$$\frac{d^2}{dt^2} \left( V_T z_c \right) - \frac{3}{2} \left( \frac{1}{R_1} - \frac{1}{R_2} \right) = 6Re^{-1}Lf, \quad (2.2)$$

where  $Re^{-1} \equiv (\mu/\rho)(\rho/r\sigma)^{1/2}$  represents the ratio of viscous to inertial forces.

Inviscid behaviour dominates the dynamics and we put  $Re^{-1} = 0$  for now in order to obtain a closed-form equation for the dissipationless motions. Viscous effects are discussed in §4. The magnitude of the centre-of-mass for each droplet  $z_i$  has a closed-form expression in terms of droplet height  $h_i$  and length  $L$ ,  $z_i = L + (1/2)h_i(2 + h_i^2)/(3 + h_i^2)$ . Droplet radii are given by  $2R_i = (h_i + 1/h_i)$  and volumes by  $V_i = (1/8)h_i(3 + h_i^2)$  (figure 2). System centre-of-mass is related to component centre-of-mass by  $z_c V_T = -z_1 V_1 + z_2 V_2$  where the tube volume drops out since its centre-of-mass stays fixed at  $z = 0$ . Substituting these relationships into (2.2), two second-order systems, each in terms of dependent variables  $h_1$  and  $h_2$ , emerge. In view of the constant-volume constraint,  $h_1$  and  $h_2$  are not independent and therefore the more convenient variables are  $(\Theta, \lambda) \equiv (V_1 - V_2, V_1 + V_2)$ . In order to express (2.2) in terms of  $(\Theta, \lambda)$ , mappings between coordinate pairs  $(h_1, h_2)$ ,  $(V_1, V_2)$  and  $(\Theta, \lambda)$  are needed. The first mapping is nonlinear (everywhere invertible, though) and the second linear. Indeed, one can build the functions

$$h_1 = H_1(\Theta, \lambda), \quad h_2 = H_2(\Theta, \lambda) \quad (2.3)$$

from the inverse  $h_i = h_i(V_i)$  of the cubic expression above; explicitly,  $h = [4V + (1 + (4V)^2)^{1/2}]^{1/3} + [4V - (1 + (4V)^2)^{1/2}]^{1/3}$ . In summary, (2.2) can be rewritten

$$\frac{d}{dt} \left( A(\Theta; \lambda, L) \frac{d\Theta}{dt} \right) + C(\Theta; \lambda) = 0, \quad (2.4)$$

where

$$A(\Theta; \lambda, L) \equiv (H_1 + H_2 + 3L), \quad (2.5)$$

$$C(\Theta; \lambda) \equiv 9 \left( \frac{(H_1 - H_2)(1 - H_1 H_2)}{(H_1^2 + 1)(H_2^2 + 1)} \right). \quad (2.6)$$

The rate of volume redistribution  $d\Theta/dt$  is multiplied by  $A$ , which accounts for the influence of tube length and spherical-cap geometries on the centre-of-mass of the system. Note that parameter  $L$  appears only in function  $A$  and serves to tune the strength of inertia. The function  $C$  represents the restoring force corresponding to a single- or double-well potential depending on whether  $\lambda < 1$  or  $\lambda > 1$ , respectively.

### 2.1. Phase-plane solution

The phase-plane is organized by the equilibria which depend on  $\lambda$ . Equilibrium solutions of (2.4) are the zeros of  $C(\Theta; \lambda)$  and can be read off as  $H_1 = H_2$  and  $H_1 H_2 = 1$ . The null solution of symmetric shapes bifurcates into the family of antisymmetric shapes at  $\lambda = \lambda_{hs} \equiv 1$  where shapes are hemispherical (hs),

$$\text{branch 1 } (H_1 = H_2) : \Theta_1^*(\lambda) = 0 \quad \text{for all } \lambda,$$

$$\text{branch 2 } (H_1 H_2 = 1) : \Theta_2^*(\lambda) = \pm \left( \lambda^2 - \frac{3}{4} \lambda^{2/3} - \frac{1}{4} \right)^{1/2} \quad \text{for } \lambda \geq 1.$$

The pitchfork bifurcation is plotted in figure 3. (Measured steady shapes compare well to the pitchfork prediction (Vogel *et al.* 2005).) Two representative phase-plane plots show the finite-amplitude behaviour. Below  $\lambda_{hs}$ , a family of limit cycles surrounds the symmetric steady state (null solution), corresponding to finite-amplitude periodic oscillations. Above  $\lambda_{hs}$ , the null solution becomes a saddle point. Small but finite-amplitude initial displacements from either the up or down equilibrium state again result in limit-cycle oscillations about that state. However, large disturbances lead to looping solutions where the system volume oscillates between being predominantly

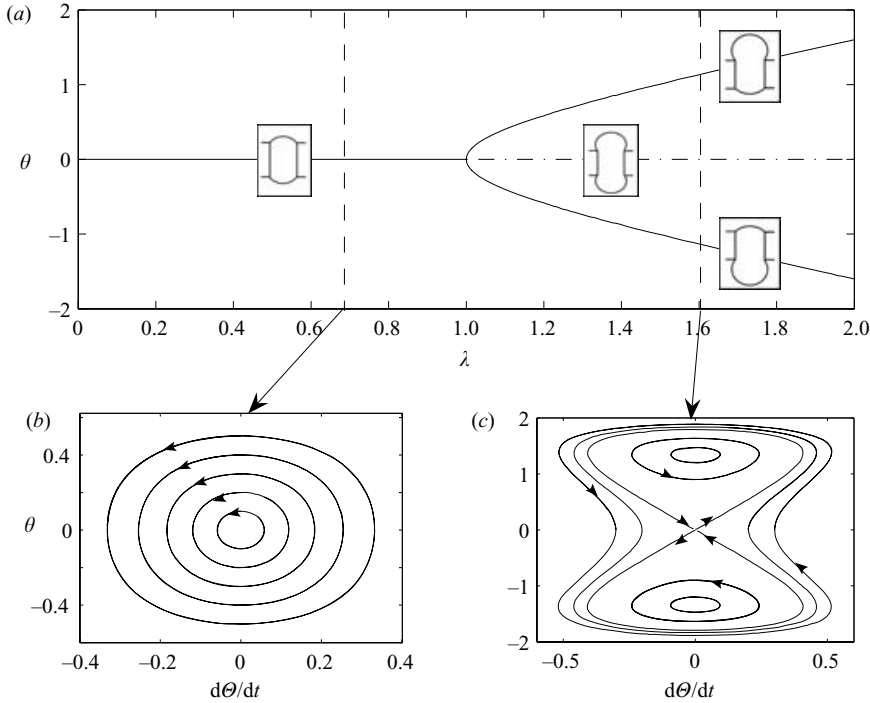


FIGURE 3. (a) Bifurcation diagram with typical equilibrium shapes sketched. Typical phase-plane solution for (b)  $\lambda < 1$  ( $\lambda = 0.70$ ) and (c)  $\lambda > 1$  ( $\lambda = 1.6$ ).

above or below the tube mid-plane. The trajectories from the saddle point at  $\Theta = 0$  define the separatrix, separating initial conditions that lead to looping solutions from those for which  $\Theta(t)$  does not change sign. This qualitative behaviour can be ascertained using stock phase-plane tools (e.g. Minorsky 1962). The solutions plotted in figure 3 were computed using a standard ODE solver (MATLAB). The phase-plane is qualitatively like that of the two-point attractor with quadratic energy wells (e.g. Thomson & Hunt 1986).

Linearizing (2.4) about a steady state in the standard way gives,  $A_* d^2\Theta/dt^2 + C_*\Theta = 0$  where  $A_*$  and  $C_*$  are coefficients that depend on  $\lambda$  through  $\Theta_i^*$ ,  $i = 1, 2$ . Eigenvalues can be read off as  $\pm\sqrt{C_*/A_*}$ . Along branch 1 and for  $\lambda < 1$ , the eigenvalues are a complex conjugate pair  $\pm i\omega_1^*$  with values (using the notation  $y \equiv H_1 = H_2$ )

$$\omega_1^{*2} = \frac{24(1 - y^2)}{(y^2 + 1)^3(2y + 3L)} \quad \text{for } y < 1. \quad (2.7)$$

For this lens-like family, droplet apex  $y$  and total volume  $\lambda$  are related by  $\lambda = \frac{1}{4}y(3 + y^2)$ . For  $\lambda > 1$ , the eigenvalues  $\pm\gamma_1^*$  are real, with values  $\gamma_1^{*2}$  obtained by replacing  $(1 - y^2)$  by  $(y^2 - 1)$  in (2.7). For the family of equilibria along branch 2 (upper), we use the notation  $y \equiv H_2 = H_1^{-1}$ . For these states, droplet height  $y$  and total volume  $\lambda$  are related by  $\lambda = \frac{1}{8}(y + 1/y)^3$ . The eigenvalues are complex conjugates  $\pm i\omega_2^*$  with values

$$\omega_2^{*2} = \frac{12(y - 1/y)^2}{(y + 1/y)^2(y + 1/y + 3L)} \quad \text{for } y > 1. \quad (2.8)$$

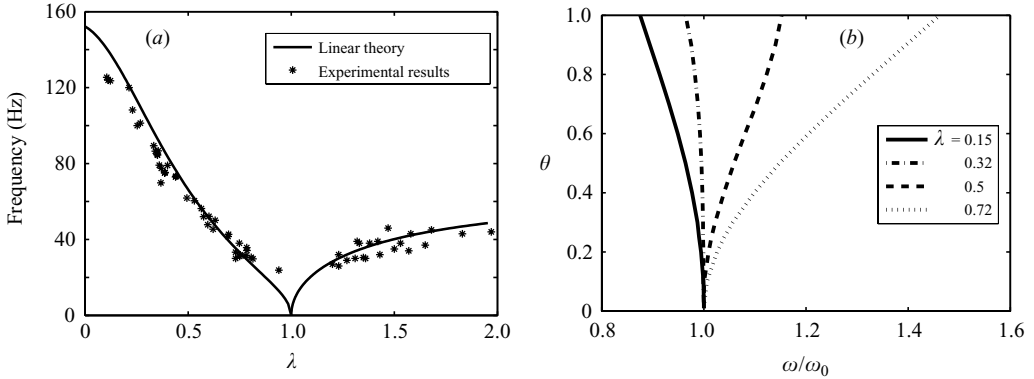


FIGURE 4. (a) Dimensional vibration frequency  $\omega_1^*$  for  $\lambda < 1$  and  $\omega_2^*$  for  $\lambda > 1$  according to linear theory (solid line) and compared to experiment (symbols). (b) Frequency of oscillation for limit cycles of amplitude  $\Theta$  scaled by the linear frequency  $\omega_0 \equiv \omega_1^*$ .  $L = 1.1$ .

For the lower segment of branch 2, replace  $y$  by  $1/y$  in (2.8) and restrict to  $y < 1$  to find the same eigenvalues, as must be the case. Note that at  $\lambda = 1$  ( $y = 1$ ) the system has a double-zero eigenvalue. The frequencies  $\omega_1^*$  (for  $\lambda < 1$ ) and  $\omega_2^*$  (for  $\lambda > 1$ ) are plotted in dimensional form as a solid line in figure 4. The data are discussed below. Linear frequencies (2.7) and (2.8) could have been reported alternatively as functions of  $\lambda$  rather than of  $y$ .

To summarize the linear behaviour, branch 1 is a centre below critical and a saddle point above critical while the upper and lower segments of branch 2, equivalent by symmetry, are centres. The transition at  $\lambda_{hs}$  does not depend on  $L$ . However the magnitudes of the eigenvalues do, with large  $L$  corresponding to slower vibration frequencies. That is, for large tube volumes, the capillary forces acting at the tube ends have a smaller influence on the centre-of-mass of the system; capillarity takes longer to restore shapes.

Although periods of oscillation for finite-amplitude limit cycles can be obtained computationally from (2.4), an analytic expression is readily derived. To this end, a first-integral of (2.4) can be written

$$\frac{1}{2} \left( A(\Theta; \lambda) \frac{d\Theta}{dt} \right)^2 + U(\Theta; \lambda) = \text{const} \equiv E, \tag{2.9}$$

where  $U(\Theta)$  is obtained by quadrature,

$$U(\Theta) = \int_0^\Theta A(s)C(s) ds. \tag{2.10}$$

It can be shown that the product of  $A(\Theta; \lambda)C(\Theta; \lambda)$  is an odd function of  $\Theta$  which leads to a  $U(\Theta)$  that is even about  $\Theta = 0$ . Solving (2.9) for  $d\Theta/dt$ , noting the separability of the variables  $\Theta$  and  $t$ , allows the period of oscillation  $T$  for a limit cycle to be expressed in closed form,

$$T = 2 \int_{\Theta_+}^{\Theta_-} \sqrt{\frac{A}{2(E - U)}} d\Theta. \tag{2.11}$$

Here  $\Theta_-$  and  $\Theta_+$  are the minimum and maximum of  $\Theta$  along the closed trajectory in the phase-plane, respectively.

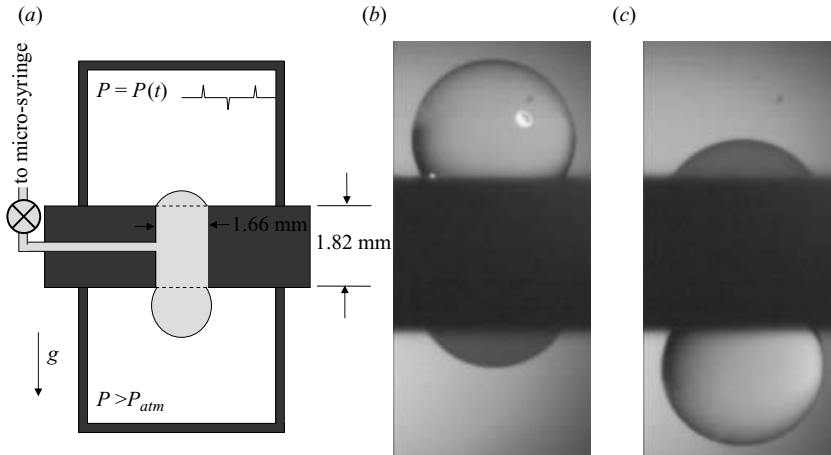


FIGURE 5. (a) Experimental set-up for droplet system with a steady pressure bias in the lower chamber and transient applied pressure pulse in the upper chamber. Images of the states when the system is bi-stable where (b) is before and (c) is after a positive pulse  $P(t)$  is applied.

For oscillations symmetric about  $\Theta = 0$  (branch 1 with  $\lambda < 1$  and the looping solutions),  $\Theta_- = -\Theta_+$  and expression (2.11) can be evaluated as the amplitude  $\Theta \equiv \Theta_+$  of the disturbance is increased. Figure 4(b) shows how the frequency changes with amplitude for sub-hemispherical droplets. For finite-amplitude oscillations, the restoring capillary force varies from soft to hard as  $\lambda$  is increased from 0 to 1.

### 3. Experimental results

The experimental set-up consists of a Teflon plate (1.82 mm thick) with a small circular hole (0.83 mm radius) bored through, as depicted in figure 5(a). A micro-syringe is used to feed water to control the volume of the droplets. Pinned contact lines are maintained well as verified through image analysis. The plate separates two pressure-controlled chambers. Gravity is weak relative to surface tension (Bond number  $B \equiv \rho g r^2 / \sigma \sim 0.1$ ) yet gravity has a non-negligible effect. It adds a hydrostatic head to the bottom droplet to make its mean pressure greater and along the length of both droplets it distorts the droplet shape from spherical. To counter the head, a pressure bias in the lower chamber is applied. Further details of the experimental set-up are given by Hirs *et al.* (2005).

We begin by fixing the total volume of the droplet then slightly adjusting the pressure bias to achieve an equilibrium state of zero volume difference. A micro-stepper motor is then used to apply a pressure pulse in one air chamber to perturb the droplet. The duration of the pressure pulse is less than 100 ms and only after this time has elapsed are the data analysed. Figure 5(b,c) shows images of the bistable droplet states at equilibrium.

Depending on the amplitude of the pulse, four different dynamical behaviours are observed in experiments: (i) small vibrations about a static shape; (ii) bi-stable oscillations that toggle up, down and so forth  $n$ -times before coming to rest (up to  $n = 5$ ); (iii) deformations that blow the liquid completely out of the tube and (iv) deformations where some liquid is left in the tube with the rest breaking off as a satellite droplet. A high-speed video camera is used to capture the droplet motions (Redlake MotionPro HS2-C-4). For large pressure pulses the initial shape deviations

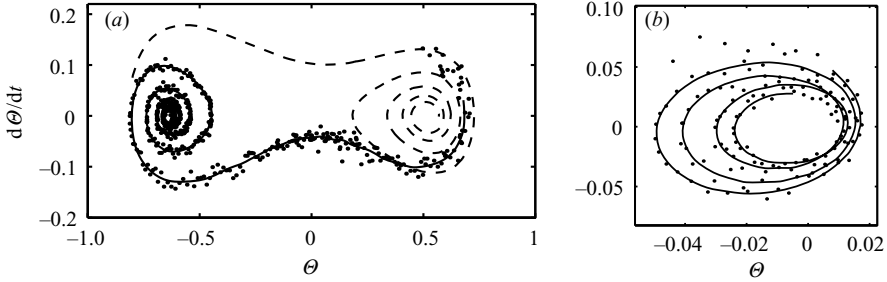


FIGURE 6. Phase-plane plots of experimental data as single frames (dots) and as time-averages over many frames (solid curves): (a) for a large disturbance that causes a toggle from droplet-down to -up ( $\lambda = 1.2$ ) and a solution of the viscous model (dashed curve) starting from initial condition of comparable magnitude (displaced for decay to the opposite equilibrium, for clarity); (b) for a small disturbance that causes vibration about the steady state ( $\lambda = 0.4$ ) where the centre is slightly off-set from  $\Theta = 0$  due to imperfect countering of gravity by the pressure bias.

of the droplets are not spherical caps (higher capillary modes are excited). However, later in the large-pulse decay and for the entire decay to equilibrium of small pulses, the spherical-cap assumption holds reasonably. Image capture with edge detection gives the droplet volumes and thereby the reported  $\Theta$  and  $\lambda$  from experiment.

Time traces  $\Theta(t)$  show damped oscillations. The role of dissipation is clearly seen in the experimental phase-plane plot corresponding to case (ii), figure 6(a). The under-damped nature of the oscillation is evident for the small-disturbance case (i), figure 6(b), where a large number of vibrations occur before the droplet settles to equilibrium. For these, by fitting to  $\exp(i\omega t)\exp(-\delta t)$  (dimensional), it is straightforward to extract the frequency  $\omega$  from the trace. Frequencies are plotted in figure 4(a) with an experimental uncertainty of a few per cent. Damping rate  $\delta$  can also be extracted but has a greater relative error, as dissipation is a lower-order effect. For completeness, we report that the damping  $\delta \sim 20 \text{ s}^{-1}$  is found to be constant to within 15% over the  $\lambda$  range. Setting  $\delta = (\mu/\rho)/\ell_v^2$  and solving for the viscous length scale gives  $\ell_v \sim 0.2 \text{ mm}$ .

#### 4. Discussion

The dynamics of a capillarity-generated centre-of-mass mode has been considered in a number of contexts, including the pendant free droplet (DePaoli *et al.* 1994) and the sloshing of liquid mass in a cylindrical tube (Bian *et al.* 2003). Strani & Sabetta (1984) considered a droplet in contact with a solid spherical-cap support – not unlike the contact that a ‘golf tee’ makes with the ball – and made a detailed comparison with Rayleigh oscillations. The droplet was surrounded by a second liquid (immiscible). The equations that Rayleigh solved were augmented with appropriate boundary conditions for the contact. They found that all the Rayleigh frequencies were modified. In addition, the constraint introduced a new low-frequency mode. This mode tends to a zero-frequency rigid displacement as the contact diminishes and tends to infinite frequency as the contact envelopes the entire surface. Hence, there is a cross-over for Strani & Sabetta’s problem. Indeed, to the extent they can be compared, all our linear frequency results are qualitatively consistent with Strani & Sabetta’s. An important difference is that their hemispherical meniscus has non-zero



frequency. This is due to the asymmetry of the constraint and precludes a quantitative comparison.

The linear frequencies we report reflect a balance between inertia and the capillary restoring force, as modified by the constraint. Increasing  $L$  generally increases the inertia of the system and decreases the oscillation frequency, as illustrated by the linear results (2.7) and (2.8). In particular, for lens-shaped interfaces on a tube (2.7), in the limit of planar shapes  $\lambda \rightarrow 0$ , the restoring force is constant and inertia controls the frequency,  $\omega_1^{*2} \rightarrow 8/L$ . The dependence on  $\lambda$  is more subtle. As  $\lambda$  increases, the frequency monotonically decreases to zero at the hemispherical state. In fact, all constrained hemispherical shapes  $\lambda=1$  have zero linear frequency. The reason for this is that the potential-well is flat to second-order at this state – it transitions here from concave-up to concave-down along the family of symmetric states. Along the antisymmetric family (2.8), the linear frequencies increase from zero, at  $\lambda=1$ , reach a maximum and then decrease back down to zero, as  $\lambda \rightarrow \infty$ . The maximum is an artifact of the scaling, however (relative to inertia, capillarity decreases due to increasing volume). Indeed, rescaling by  $\omega_2$ , cf. (1.1), shows a monotone increasing frequency from the hemispherical shape, according to

$$(\omega_2^*/\omega_2)^2 = \frac{3}{16} \frac{(y + 1/y)(y - 1/y)^2}{(y + 1/y + 3L)} \quad \text{for } y > 1. \quad (4.1)$$

Hence, there is only one  $\lambda_c$  below which the constrained sphere ( $L=0$ ) has lower frequency than the unconstrained one (same volume). The value  $y_c \sim 2.68$ , reported in §1, corresponds to  $\lambda_c \sim 3.55$  and we see that all the measured frequencies are below the lowest Rayleigh frequency (figure 4a).

Scaling  $\omega_1^*$  with the Rayleigh frequency  $\omega_2$  corresponding to the same volume yields

$$(\omega_1^*/\omega_2)^2 = \frac{3}{4} \frac{y(y^2 + 3)(1 - y^2)}{(y^2 + 1)^3(2y + 3L)} \quad \text{for } y < 1. \quad (4.2)$$

Note that, in this scaling, the limit  $\lambda=0$  is a singular limit due to the vanishing of the scaling volume. This form may nevertheless be useful to the practitioner.

Finite-amplitude oscillations can have frequencies that are higher or lower than their linear counterparts, as predicted in figure 4(b). The softening/hardening can be understood in terms of the nonlinearity of  $C(\Theta)$  (2.6) which shows softening-spring behaviour for smaller volumes and hardening for volumes nearer hemispherical. Alternatively, the effect can be seen in the potential  $U(\Theta)$  (2.10) and how its landscape changes with  $\lambda$ .

So far, the relevance of the model is based on comparison to measured frequencies. Linear frequencies are in quantitative agreement over a decade of volumes (figure 4a). The range of volumes tested in experiment is limited by the contact pinning. As we shall now explain, it turns out that measured viscous dissipation is also consistent with (2.2) written in terms of  $\Theta$ ; that is, with the viscous extension of (2.4),

$$\frac{d}{dt} \left( A(\Theta) \frac{d\Theta}{dt} \right) + C(\Theta) = 18Re^{-1}Lf \left( \frac{d\Theta}{dt}, \Theta \right). \quad (4.3)$$

In contrast to  $A$  and  $C$ , the dependence of  $f$  on  $\Theta$  and  $d\Theta/dt$  is not known. Nevertheless, for the linearized version of (4.3), which governs the decay of small-amplitude disturbances, there is only a single unknown coefficient  $f_*$ ,

$$A_* \frac{d^2\Theta}{dt^2} + C_*\Theta - 18Re^{-1}Lf_* \frac{d\Theta}{dt} = 0. \quad (4.4)$$

The damping of (4.4) can be fitted to the measured  $\delta \sim 20 \text{ s}^{-1}$  (§3) to find  $f_* \sim 3.4$ . A criterion for neglecting viscous effects emerges: that the coefficient of the damping term be small relative to that of the inertia term in (4.4) requires  $Re \gg 60L/A_*$ . For the range of  $\lambda$  where there are measurements,  $A_* \sim 5$ , and the criterion becomes  $Re \gg 13$ . For water and our tube size,  $Re \sim 240$ , suggesting that inertia dominates but that viscous effects are nonetheless non-negligible – all consistent with observation.

Viscous influence has been measured in the context of small disturbances from equilibrium. In an *ad hoc* fashion, we now replace the nonlinear viscous force in (4.3) with the *linear* term  $18Re^{-1}Lf_*d\Theta/dt$ . That is, the nonlinear evolution equation (2.4) is generalized to include linear viscous effects. This damped nonlinear ODE is solved starting from an initial condition comparable in magnitude to that for the experiments to obtain the trajectory seen in figure 6(a). To sum up, not only does the finite-amplitude behaviour exhibit dynamics in qualitative agreement with the inviscid model (figure 6), but the influence of dissipation is also captured (with no free parameters) by a linear damping term with coefficient measured from small-amplitude data.

In comparing experiment to model, the neglect in the latter of (i) gravity, (ii) deformations that are not spherical-shaped, and (iii) viscosity are the three most significant idealizations. Viscous effects (iii) have just been discussed. Regarding (i), the pressure bias applied in the experiment serves to adjust the position of the zero-reference for the hydrostatic head but does not eliminate shape distortions due to gravity. Including gravity as a perturbation from zero Bond number would be a straightforward extension – one that might destroy much of the simplicity of the present model, however. Regarding (ii), the restriction to spherical-cap deformations is reasonably valid for small disturbances. For large pressure pulses, the droplets clearly deform from spherical shapes and can take the form of pendent drop oscillations, similar to those reported in Basaran & DePaoli (1994). These higher-frequency secondary vibrations may influence how fluid is exchanged between the droplets. However, these modes quickly dissipate (usually within the duration of the pressure pulse, 100 ms) and the spherical-cap shapes are recovered.

In summary, the different dynamics predicted by a capillarity/inertia model with spherical-cap deformations are faithful to observation. Viscous damping (included as a model extension) and non-spherical shapes are lower-order effects for the parameters considered.

NASA NAG3-2713, -2714, NSF DMI-0500311, -0500408, ARO and DARPA are thanked.

#### REFERENCES

- BASARAN, O. & DEPAOLI, D. 1994 Nonlinear oscillations of pendant drops. *Phys. Fluids* **6** (9), 2923–2943.
- BIAN, X., PERLIN, M., SCHULTZ, W. & AGARWAL, M. 2003 Axisymmetric slosh frequencies of a liquid mass in a circular cylinder. *Phys. Fluids* **15** (12), 3659–3664.
- BISCH, C., LASEK, A. & RODOT, H. 1982 Comportement hydrodynamique de volumes liquides sphériques semi-libres en apesanteur simulée. *J. Méc. Théor. Appl.* **1**, 165–184.
- DEPAOLI, D., FENG, J., BASARAN, O. & SCOTT, T. 1994 Hysteresis in forced oscillations of pendant drops. *Phys. Fluids* **7** (6), 1181–1183.
- HIRSRA, A. H., LÓPEZ, C. A., LAYTIN, M. A., VOGEL, M. J. & STEEN, P. H. 2005 Low-dissipation capillary switches at small scales. *Appl. Phys. Lett.* **86**, 014106.
- LAMB, H. 1932 *Hydrodynamics*, 6th edn. Cambridge: Cambridge University Press.

- LÓPEZ, C. A., LEE, C.-C. & HIRSA, A. H. 2005 Electrochemically activated adaptive liquid lens. *Appl. Phys. Lett.* **87**, 134102.
- MINORSKY, N. 1962 *Nonlinear Oscillations*. Van Nostrand.
- RAYLEIGH LORD 1879 On the capillary phenomena of jets. *Proc. R. Soc. Lond. A* **29**, 71–97.
- STRANI, M. & SABETTA, F. 1984 Free vibrations of a drop in partial contact with a solid support. *J. Fluid Mech.* **141**, 233–247.
- THOMSON, J. & HUNT, G. 1986 *Nonlinear Dynamics and Chaos: Geometrical Methods for Engineers and Scientists*. John Wiley and Sons.
- TRINH, E. & WANG, T. G. 1982 Large-amplitude free and driven drop-shape oscillation: experimental observations. *J. Fluid Mech.* **122**, 315–338.
- VOGEL, M. J., EHRHARD, P. & STEEN, P. H. 2005 The electroosmotic droplet switch: Countering capillarity with electrokinetics. *Proc. Natl Acad. Sci.* **102**, 11974–11979.
- WEBB, R. 1880 Some applications of a theorem in solid geometry. *Mess. Math.* **IX**, 177.